Controlling photocatalytic activity by self-assembly – tuning perylene bisimide photocatalysts for the Hydrogen Evolution Reaction

Daniel McDowall,[a] Benjamin J. Greeves,[b] Rob Clowes,[c] Kate McAulay,[a] Ana M. Fuentes-Caparrós,[a] Lisa Thomson,[a] Nikul Khunti,[d] Nathan Cowieson,[d] Michael C. Nolan,[a,b] Matthew Wallace,[e] Andrew I. Cooper,[c] Emily R. Draper,[a] Alexander J. Cowan[b,*] and Dave J. Adams[a,*]

[a] School of Chemistry, University of Glasgow, Glasgow, G12 8QQ, U.K.

[b] Stephenson Institute for Renewable Energy and the Department of Chemistry, University of Liverpool, Liverpool, L69 7ZF, U.K.

[c] Department of Chemistry, University of Liverpool, Crown Street, Liverpool, L69 7ZF, U.K.

[d] Diamond Light Source Ltd, Harwell Science and Innovation Campus, Didcot, OX11 0QX, U.K.

[e] School of Pharmacy, University of East Anglia, Norwich Research Park, Norwich, NR4 7TJ, U.K.

DM and BJG contributed equally to this work.

Abstract

Amino acid functionalised perylene bisimides (PBIs) form self-assembled structures in solution, the nature of which depends on the local environment. Using a high throughput photocatalysis set-up, we have studied five PBIs for the hydrogen evolution reaction (HER) under a range of conditions (pH and hole scavenger concentration) across 350 experiments to explore the relationship between supramolecular structure and photocatalytic activity. Using small angle X-ray scattering (SAXS), NMR spectroscopy and UV-Vis absorption spectroscopy we show that photocatalytic activity is determined by the nature of the self-assembled aggregate that is formed, demonstrating the potential of self-assembly to tune activity. There is a clear correlation between the presence of charged flexible cylindrical aggregates and the occurrence of photocatalytic H_2 production, with UV-Vis spectroscopy indicating that the most active structure type has distinctive form of π-aggregation which we propose enables efficient charge separation across multiple PBI units.

Introduction

Perylene bisimides (PBIs) are very useful molecules, having excellent mechanical, electrical and optical tuneability and they have been used for a wide range of energy related

applications.[1–3] There are a wide variety of different PBIs reported.[3–7] PBIs are usually strongly absorbing in the visible light region and many possess n-type semiconductor behaviour when aggregated.[8,9] PBIs often self-assemble in solution at high concentrations or when given a suitable trigger. They typically self-assemble into one-dimensional (1D) structures such as nanofibres or nanotubes, a process driven by non-covalent interactions such hydrogen bonding, van der Waals interactions and π-π stacking.[2,3,10–13,14] The electronic properties of PBIs can be tuned by how they are functionalised and by the type of self-assembled aggregate that is formed.[10,15]

Using solar energy to generate H_2 and O_2 from water is highly desirable to form part of a "green economy".[16–18] H_2 can be used as a fuel for combustion, within fuel cells and both H_2 and O_2 are also important chemical feedstocks.[17,18] PBIs and the related perylene monoimides (PMIs) have shown promise in the utilisation of solar energy to drive chemical reactions, and have been shown to be able to act as effective photocatalysts for both H_2 evolution and O_2 evolution reactions.[19–23] Some of these systems use perylene mono or bis imides in a self-assembled state, but other self-assembled photocatalysts have been reported.[24] Often PBIs are designed for solubility in organic solvents but they can be dispersed in water using a range of suitable functional groups including oligoamines, oligo(ethylene oxide)s, charged species such as sulfonates and amino acids at the imide position (Figure 1).[10,25,26] Many amino acid functionalised PBIs have been reported and can form self-assembled structures in aqueous solution or form hydrogels depending on the exact conditions used.[6,25,27–30] Free carboxylic acids on the amino acids mean that the PBIs can be dispersed in water at a pH above the pK_a and then often form hydrogels when the pH is lowered below the pK_a.[31,32] The application of hydrogels and aqueous solvated self-assembled materials to photocatalysis is particularly interesting as we have recently shown that the solvent environment enables charge separation, overcoming a known limitation of many other organic photocatalysts with inherently low dielectric constants.[33]

Stupp's group has shown a range of self-assembled PMIs can be effective as part of a photocatalytic hydrogen evolution reaction (HER).[20,34–36] Recently, they have also published work studying hybrid polyelectrolyte and supramolecular systems in which PMIs are entrapped in a crosslinked polyelectrolyte hydrogel.[37] Once deposited in the hydrogel network, self-assembly of the PMI is triggered through a solvent switch and the photocatalytic hydrogen production of these systems studied. Interestingly, they note a pH dependence, where the H_2 production increases from pH 1.8 to 4.0.[37] In other work, visible-light-driven H_2 evolution from water has been performed using 1D nanofiber composites with dodecyl and/or dimethylaniline functionalised PBIs.[21] The PBI with the dimethylaniline substituent showed greater H_2

evolution, which was attributed to the electron donating characteristics of the dimethylaniline improving charge separation.[21]

Some of us have used a phenylalanine functionalised PBI (PBI-F) as a self-assembled photocatalyst for the HER,[22] where the activity was greatly dependent on solution pH. PBI-F forms hydrogels at low pH (< pH 5.0), and this coincided with optimal activity in the HER at pH 4.0. The pH was lowered while stirring, resulting in the same self-assembled structure present in a hydrogel but not a self-supporting network. The evolved H_2 required the formation of 1D structures. Although this study allowed us to propose that the nature of the supramolecular structures formed was important in determining activity, our suggestion was based off this single example, and why a specific supramolecular structure was needed was not examined. To address this here we significantly expand the library of PBIs and conditions studied to allow for identification of wider supramolecular structure-activity trends.

A challenge, and potential advantage, of developing self-assembled photocatalysts is that the nature of the self-assembled structure formed in such systems is often determined by (and sensitive to) a significant number of variables. These include pH, concentration, co-solvent (methanol is present as a sacrificial electron donor, but will also affect the solubility of the PBI), temperature, salts, and additives.[38–40] Therefore a single sub-unit can assemble into a wide range of photocatalyst structures. However, identifying and controlling the formation of the most active structures remains challenging and optimising even a single system is extremely time-demanding and it is unsurprising that there is a tendency in the literature to focus on a small number of experimental variables. This may lead to effective photocatalytic systems being missed simply due to time constraints.

To address this, here we set out to use a high throughput approach to allow us to access a wider range of experimental parameters.[41] From five PBIs we found three that form structures that are active for the photocatalytic evolution of H_2. The three active PBIs show a pH dependent activity, with maximum hydrogen evolution at pH 5.0. The two other PBIs showed very little H_2 evolution but the activity in the HER still shows a pH dependence. Once optimal conditions for HER had been identified it was possible to deploy a range of characterisation techniques and we show a clear correlation between the presence of charged flexible cylindrical aggregates and high levels of H_2 being formed demonstrating a wider link between supramolecular structure and photocatalytic activity.

Results and discussion

A small library five different PBIs were prepared varying the amino acid at the imide positions was used for this study (Figure 1), but under a wide range of conditions leading to ~350

photocatalytic experiments being carried out. Dispersions of these PBIs can be formed at high pH by the addition of a base to an aqueous suspension of the PBIs.[6,22] Samples at different pH were prepared by the addition of dilute acid to the stock solutions at high pH. These PBIs can form gels at low pH.[6,22] At pH >5.0, UV-Vis absorption spectroscopy shows that the PBIs exist as aggregated structures due to the presence of strong π-π interactions. Only at concentrations of $<10^{-6}$ M are free PBI molecules seen (Figure S2). Therefore, at the concentrations used in this work, aggregated structures are present in vast excess.

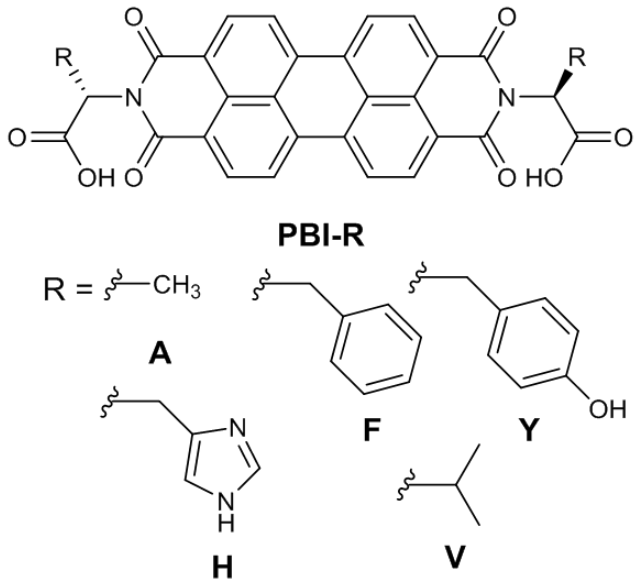

Figure 1. *Chemical structures of the PBIs studied. Letter denote the different amino acid used in the synthesis are referred to as PBI-A, PBI-F, PBI-H, PBI-V and PBI-Y in this study.*

A high throughput method was used to study photocatalytic activity (Figure 2) which enabled the activity study to be completed in ~ 2 weeks. In contrast if each sample was looked at in turn, we estimate it would take ~6 months (based on 3 hr $sample^{-1}$ and a 40 hr working week). Our aim here is not report a one off, best-in-class material, but instead to survey a wide parameter space and identify wider structure-activity trends. Briefly in the high throughput method, aqueous solutions of the PBIs (5 mg/mL) at different pH were prepared in the presence of methanol (20 v/v%), with the inclusion of Pt nanoparticles (1 mol%, average hydrodynamic diameter 16.6 ± 1.1 nm, Section 2.2 supporting information). We use methanol as a sacrificial electron donor as it is photo-stable and allows for studies across a wide pH range. While PBIs can form gels at low pH, the pH of the solutions was adjusted while stirring. This resulted in the formation of supramolecular structures, but not a self-supporting gel network. 48 samples at a time were placed on a mechanical roller and illuminated for 3 hours

under a solar simulator. Headspace gas analysis using an autosampler was used to quantify the amount of H_2 produced.

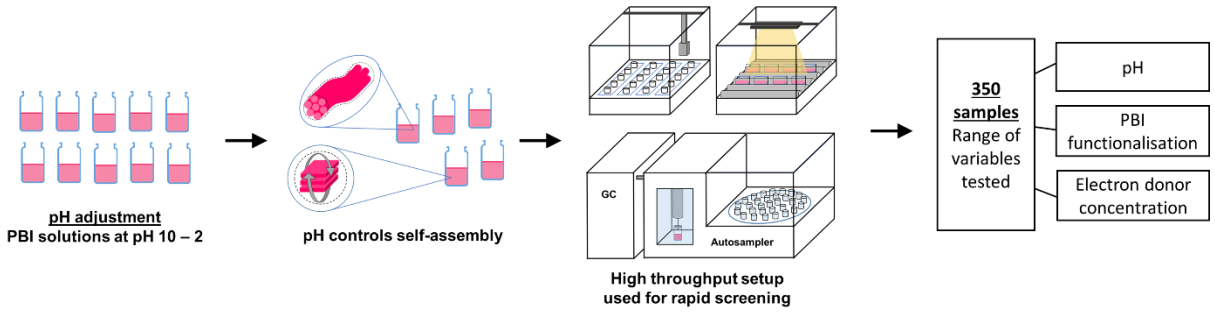

Figure 2. *Summary of the high throughput apparatus and procedure used to rapidly screen supramolecular structures. 48 samples were examined in parallel at a time.*

H_2 production was seen in significant amounts for PBI-A, PBI-F and PBI-V (Figure 3). Hydrogen was only produced in negligible amounts for PBI-H and PBI-Y. For PBI-A, PBI-F and PBI-V, the H_2 produced varied significantly with the solution pH, where the maximum H_2 was produced at pH 5.0 for all three PBIs. Similar amounts of H_2 were produced at pH 5 for both PBI-F and PBI-V, at 11.6 ± 1.1 µmol/g/hr and 12.7 ± 2.9 µmol/g/hr respectively. At pH 5, PBI-A produced 5.1 ± 1.8 µmol/g/hr H_2. As the pH was decreased from pH 5.0 to pH 2.0, the absolute amount of H_2 produced decreased, reaching a negligible amount at pH 2.0 for all three of these PBIs. At pH 6.0 and above, there was minimal H_2 produced for all three PBIs. For PBI-F, these results are consistent with previous results[22] although the absolute amount of H_2 evolved differs due to the photocatalysis set-up used. PBI-F was included in the initial high throughput screen to benchmark against conventional photocatalyst testing methods. As PBI-F has been previously reported and its behaviour is reproducible and has been previously discussed,[22] for the remainder of this study we focus the discussion and characterisation on the new samples, in particular PBI-A as a representative of a photocatalytically active material and PBI-Y as an inactive material.

PBI-A shows both UV and visible light driven H_2 production (Figure S2b) and we see no evidence for PBI degradation during a typical experiment (Figure S4,5). We propose that excitation of the PBI leads to exciton formation, followed by rapid quenching with sacrificial electron donation occurring from the methanol present. Recent spectroscopic studies on related PBI-A hydrogel films and pH 9 solutions indicate that hole transfer can occur via the alanine group and this may also be occurring here prior to methanol oxidation.[33] Electron transfer to the Pt co-catalyst from the PBI structures can then occur, enabling H_2 production. Electrochemical measurements show that H_2 evolution is thermodynamically feasible following electron transfer from the singly ($PBI^{\bullet-}$) and doubly reduced (PBI^{2-}) species below pH 8 ($PBI^{\bullet-}$

) and pH 7 (PBI^{2-}) for PBI-A, and below pH 7 ($PBI^{\bullet-}$) and pH 6 (PBI^{2-}) for PBI-Y, (Section 4.2 in the Supporting Information). However, no correlation between the measured reduction potentials of the PBI units and the level of H_2 produced, which shows a peak at pH 5, is seen. This indicates that the pH dependence alone is not due to the driving force for charge transfer from the singly ($PBI^{\bullet-}$) and doubly reduced (PBI^{2-}) species.[42,43]

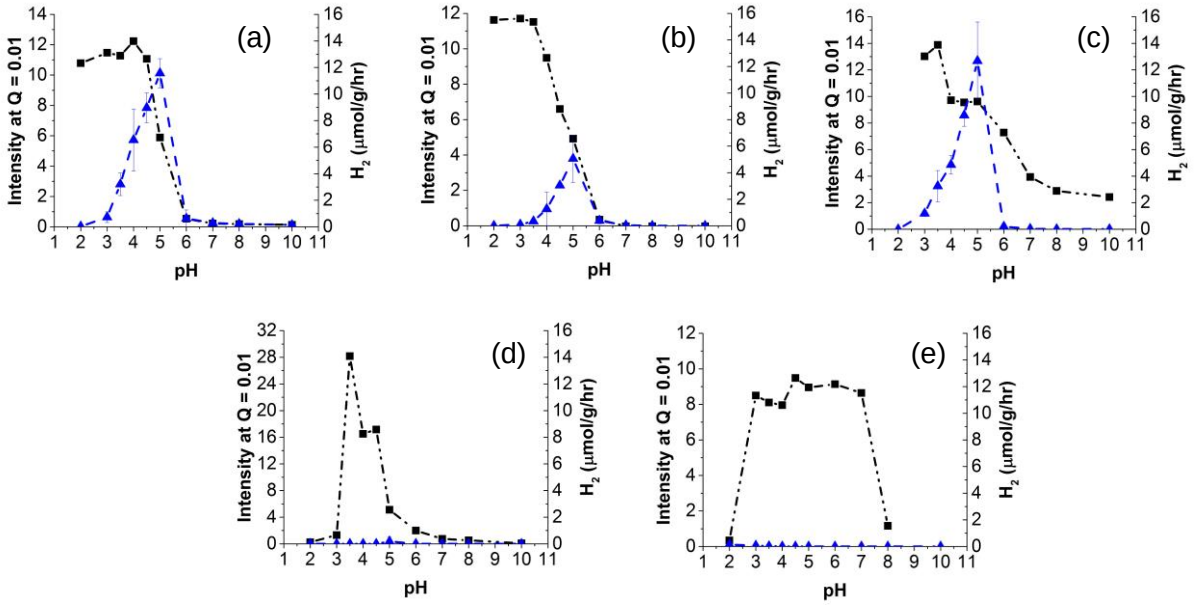

Figure 3. *Photocatalytic H_2 evolution (blue triangles) comp ared to the scattering intensity at low Q (black squares) across the pH range for (a) PBI-F; (b) PBI-A; (c) PBI-V; (d) PBI-Y and (e) PBI-H. PBI suspensions for the photocatalysis were 5 mg/mL with methanol (20 v/v %) and platinum nanoparticles (1 mol%). H_2 evolution error bars obtained from the standard deviation of samples run in triplicate.*

In addition to acting as an electron scavenger, methanol can change the solubility of PBI and its differing properties as a solvent can affect both the structure of the aggregates and the photophysics of the material. To explore the possible wider role of methanol concentration on photocatalytic activity and structure we have expanded our study to use six methanol concentrations (0 v/v%, 5 v/v%, 10 v/v%, 20 v/v%, 30 v/v% and 40 v/v%) at a constant PBI concentration of 5 mg/mL across a range of pH's for PBI-A and PBI-Y (Figure 4 and Figures S9,10 in the Supporting Information).

Regardless of the methanol concentration used, we find that both PBI-A shows the maximum level of photocatalytic H_2 evolution from pH 4.0 to 5.0, in agreement with the initial screen of PBIs and pH (Figure 4). The activity of PBI-Y remains low at all pH's and methanol concentrations studied. Between pH 4.0 and 5.0, the rate of H_2 evolution of PBI-A shows a considerable methanol dependence. Considerably less H_2 is formed when there is no

methanol present; this confirms the importance of the sacrificial electron donor indicating that in the absence of methanol the fast carrier recombination occurs preventing photoelectron transfer to the Pt co-catalyst, in agreement with past transient absorption studies on related systems.[33] The low-levels of H_2 seen at 0 v/v% may indicate that in the absence of an electron donor complete water splitting can occur or more likely that self-oxidation of the photocatalyst can take place under these conditions. The maximum H_2 evolved occurred at 30 v/v% methanol concentration, however we do not see a simple trend for increased H_2 evolution with methanol concentration and a local maximum in H_2 production is observed around 5-10 v/v% as well (Figure 4).

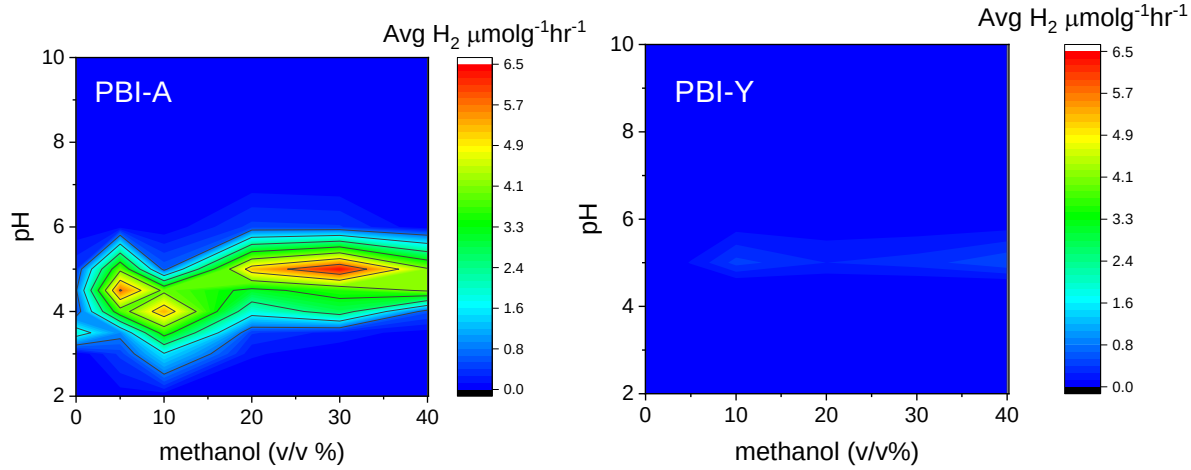

Figure 4. *Contour maps showing the rate of photocatalytic hydrogen evolution against solution pH, across a range of methanol concentrations for PBI-A PBI-Y, 5 mg/ml PBI and platinum nanoparticles (1 mol%). Each plot is composed of data from 130 samples. Dark blue areas indicate no hydrogen evolution, scaling to red where the highest rate was achieved.*

We propose that the supramolecular structures formed at different pH and methanol concentrations are key in understanding the photocatalytic activity trends. To identify the supramolecular structures formed, small angle X-ray scattering (SAXS) was used. This is an excellent technique for studying structures *in situ* as it does not require drying of the samples, which can alter the supramolecular structures present.[31] SAXS data were collected for all of the PBIs at ten different pH values as well as a range of methanol concentrations for PBI-A and PBI-Y. From the results (Figure 3 and 5; extended discussion and data shown in Section 4.4 of the Supporting Information), it can be seen that the underlying self-assembled structure changes significantly across the pH range for each PBI. The samples prepared between pH 6.0 and 10.0 had no visible large aggregates; for these samples, the SAXS generally shows lower intensity scattering. Below pH 6.0, aggregates were visible by eye and the scattering

intensity increased for all samples at low scattering vectors (Q), indicative of larger supramolecular structures forming at lower pH. A comparison between the rate of photocatalytic hydrogen evolution and the scattering intensity at low Q (0.01 $Å^{-1}$; scattering at this Q is indicative of large structures) shows a correlation for PBI-A and PBI-V (Figure 3). Between pH 6.0 to pH 5.0, we find the "switching on" of the H_2 evolution is accompanied by a large increase in scattering intensity at low Q. PBI-Y shows a similar pH dependent change in the scattering intensity at low Q but is photocatalytically inactive. For PBI-H, the H_2 evolution is also very low (within error zero) and the scattering at low Q being similar from pH 7 to 3, with a significant decrease at pH 2. We therefore demonstrate that H_2 is only produced in appreciable quantities under conditions where large supramolecular aggregates are present in high concentrations and at pH values where our electrochemical measurements indicate that H_2 evolution is thermodynamically feasible (pH < 8). This is similar to our previous observations with PBI-F where H_2 evolution required the formation of large aggregated structures indicating a wider trend with these PBI's.[22]

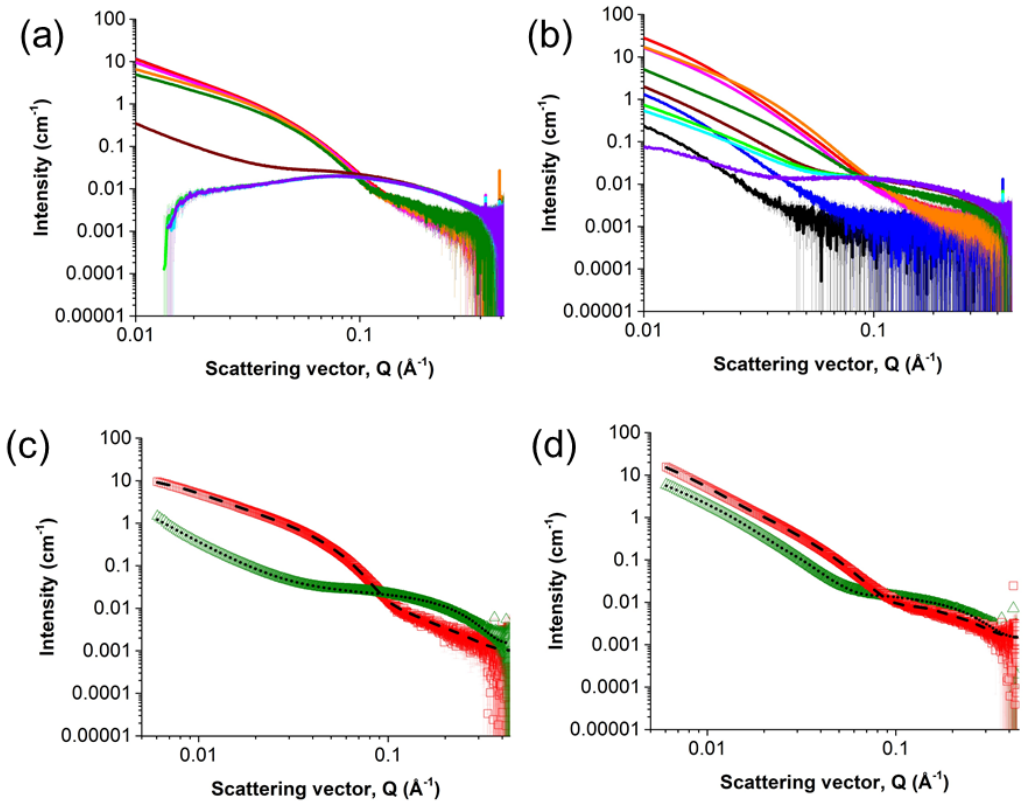

***Figure 5**. SAXS data of scattering vector vs scattering intensity for (a) PBI-A and (b) PBI-Y at pH 2 (black), pH 3 (blue), pH 3.5 (red), pH 4.0 (pink), pH 4.5 (orange), pH 5.0 (dark green), pH 6.0 (dark red), pH 7.0 (green), pH 8.0 (light blue) and pH 10.0 (purple). SAXS data at pH 5 (red squares) and 6 (green triangles) with the corresponding structural model fits (pH 5 fit dashed lines and pH 6 fit dotted lines) for (c) PBI-A and (d) PBI-Y.*

Fitting of the SAXS data to structural models was carried out using the SasView software.[44] Full fitting parameters for the PBI's are found in the supplementary information (section 4.4) and only the key points are highlighted here. For PBI-A at high pH (10 to 6), the data can be fitted to a sphere with a radius of 1 nm which is consistent with a small PBI aggregate of 2 to 6 stacked units rapidly tumbling in solution, based on an interlayer spacing of 3 – 4 Å.[7] The scattering is essentially unaffected until pH 6.0, where the data could be best fitted to a combined model of a sphere and a power law, representing a sphere of 1 nm radius and a power law of 2.6. The need to include the power law to fit the data at low Q suggests that more aggregation is beginning at this pH value. At pH 5.0, the data were best fitted to a combined model of a flexible cylinder (with a polydispersity in the radius) and a sphere. The polydispersity allows for a size distribution of cylinder radii to be accounted for in the fit. A good fit to the data could not be achieved with solely a cylinder model due the presence of a small bump at high Q. The requirement for a sphere model is attributed to the small aggregates that have yet to assemble into the larger structures that dominate the scattering data as pH is lowered further. At pH 5.0 the flexible cylinders have a length of 130.0 ± 0.5 nm, Kuhn length of 22.0 ± 0.1 nm and a radius of 3.5 ± < 0.1 nm (polydispersity 0.25). At pH 4.0 and 4.5, the data were fitted exclusively to a flexible cylinder model with a polydispersity of radius. At pH 3.5 and below, the data were fitted to a combined model of a flexible cylinder and a power law. Here the power law allowed for the fit to capture an increase in scattering at low Q. This additional scattering may be due to scattering off the fibre network, which is anticipated to form as the hydrogel forms. These data show that there is a structural transition, which begins at around pH 6.0, with 1D structures being formed at pH 5.0 and below. These data are consistent with our previous studies on PBI-A[45] and can be summarised by the cartoon in Figure 6. Fitting also reveals that for the other photocatalytically-active sample (PBI-V), the increase in scattering at low Q (Figure 3) below pH 6 is due to the formation of 1D cylindrical structures (Figure S15).

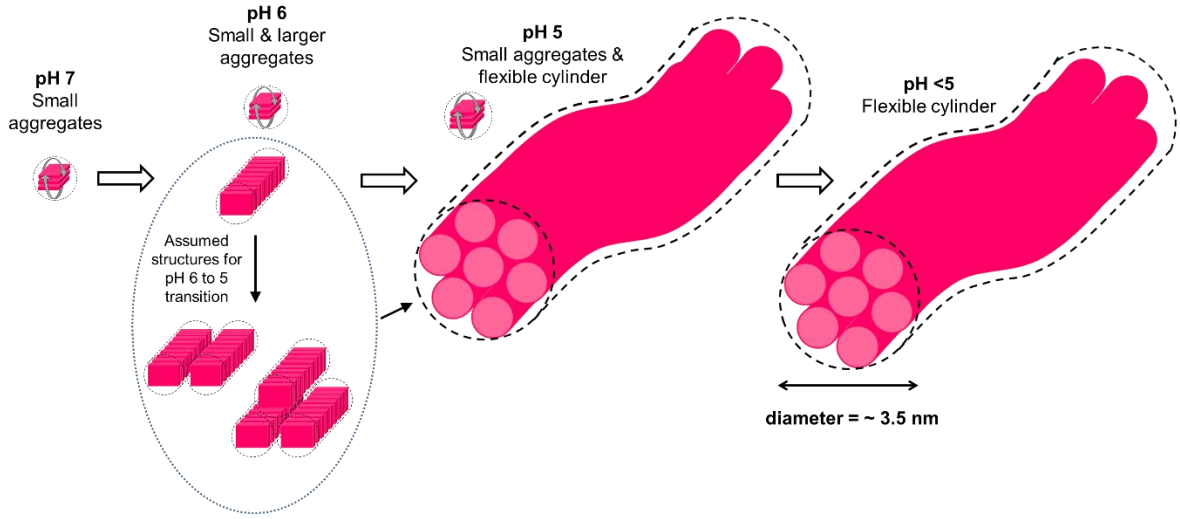

Figure 6. *Cartoon representation of the structural changed undergoing from pH 7.0 to pH <5.0 for PBI-A giving rise to the photocatalytically-active flexible cylinders. The cartoon is to scale with regards to the cross-sectional diameters of the structure. The structures obtained from SAXS fitting are represented by the black dashed lines. The structures in pink within these are assumed and to scale based on the approximate size of a PBI-A molecule. The structures in the blue oval at pH 6.0 are assumed transition structures and are not obtained from any model fitting.*

The SAXS data for the inactive PBI-Y sample showed similar trends to PBI-A. At pH 10.0, the data were best fitted to spheres of 1 nm and a power law of 1.9 indicating the presence of larger aggregates. Again, as the pH was decreased larger aggregates form with data fitted to either a combined flexible elliptical cylinder and sphere model (pH 6.0 to 5.0) or solely a flexible elliptical cylinder (pH 4.5) model, (Figure 5b and d). Below pH 4.5 the scattering intensity drops significantly for PBI-Y likely due to precipitation, leading to less sample being in the beam. PBI-H is discussed in detail in the supporting information (Figure S11), briefly we also find that the data can be well fitted to a combination of flexible cylinders and spheres. The recognition that both PBI-H and -Y, both very poor photocatalysts, form the type of large flexible cylindrical structures seen to be active with PBI-A and –V is significant.

The SAXS studies demonstrate photocatalytic H_2 evolution requires the formation of long, flexible, cylindrical supramolecular aggregates. However, SAXS is unable to identify why we observe significantly lower H_2 evolution yields with PBI-Y and –H, both of which also form similar cylindrical structures, or why the system is so sensitive to the methanol concentration. The SAXS data for PBI-A at a range of methanol concentrations for pH 2.0, 4.5 and 7.0 (see

Section 4.4.5 of the Supporting Information) show no significant changes in the type of large structures present.

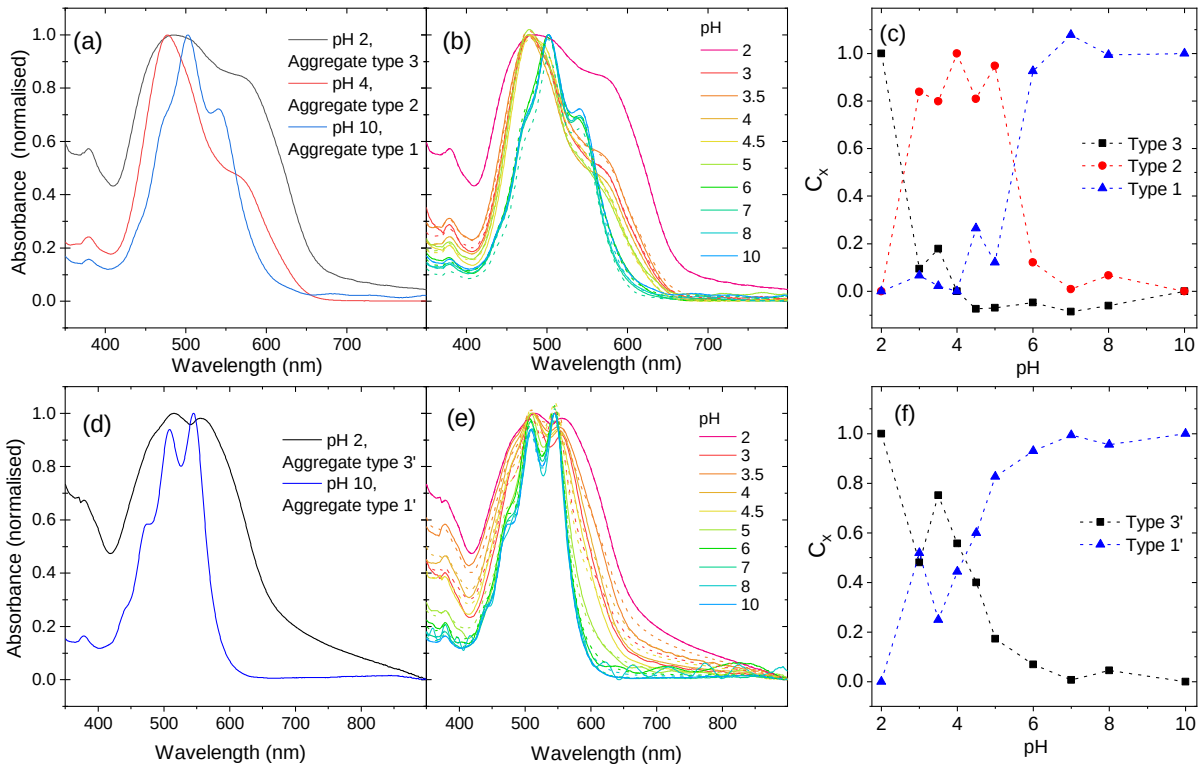

Figure 7. *UV-Vis spectra of photoactive (a) PBI-A and inactive (d) PBI-Y at selected pH values that represent distinct aggregate types. The spectra at all pH values of (b) PBI-A and (e) PBI-Y can be fitted to a linear combination of the spectra shown in panels (a,d) using equation 1, experimental data is shown with solid lines, fits dashed lines (c,f). The coefficient for each component spectrum used in the fitting of the is plotted in (c) PBI-A and (f) PBI-Y. Spectra are recorded in the presence of 20 v/v% methanol, 1% Pt, at 5 mg/ml PBI.*

Therefore, a UV-Vis absorption study was conducted to study the local electronic environment of the self-assembled PBI's at different pH (Figure 7 and Figures S18-21 in the Supporting Information). SAXS is an excellent probe of large structures whereas UV-Vis absorption spectroscopy probes the assembly of the PBIs at the molecular level and can provide information on the nature of the packing and coupling between aggregated chromophores. Initially we examine the UV-Vis spectra of PBI-A. Absorption data is recorded with PBI samples are at 5 mg/mL in the presence of 20 v/v% methanol and 1% Pt to match photocatalytic conditions. At this concentration, solutions are very strongly coloured and spectra in transmission mode could only be recorded by creating thin films by pressing

samples between two optical windows without the use of a spacer making it impossible to maintain a constant pathlength between samples. Therefore, the absorption data is normalised. The spectra for PBI-A at 3 pH values is initially discussed (10, 4, 2), Figure 7a. The spectra of PBI-A at pH 10.0 at a concentration of 5 mg/mL shows a decrease in the ratio of the first two vibronic peak intensities in the spectrum of PBI-A compared to that recorded at 10^{-6} M (Figure S2), a feature often taken to indicate H-aggregate formation,[46] however no hypsochromic shift of the peaks occurs and there is minimal spectral broadening suggesting that the degree of electronic coupling between PBI sub-units at this pH is not large.[47] Previous studies have reported the presence of relatively sharp PBI absorption bands when small PBI aggregates are present,[48] and our findings are in agreement with the fitting of the SAXS data at pH 10.

At pH 4.0, we observe significant spectral broadening and shifts in peak positions, with both hypsochromic shifted bands (502 nm at pH 10 to 478 nm pH 4) and a broad bathochromically shifted band at 571 nm appearing. These spectral features have been reported to be indicative of the formation of a face-to-face π stacked aggregates.[47] It is well known that for 1D π-π aggregated molecules that bathochromic or hypsochromic shifts in the vibronic structure of the S_0 to S_1 transition are indicators of J or H aggregate formation respectively. Rotational displacement of substituted PBI's can accompany face-to-face stacking, leading to a relaxation of the selection rules and both bathochromic and hypsochromic shifts can be observed in the aggregates.

At very low pH (pH 2.0) we see a further change in the UV-Vis spectrum indicating additional changes in the local PBI structure within the flexible cylindrical structures present. Further broadening of the UV-Vis spectrum occurs at pH 2 when compared to pH 4, likely in part at least, due to the high levels of aggregation between the supramolecular structures. Such behaviour was identified in the SAXS data where it was necessary to introduce a power law component to account for the formation of networks of fibres. Using an approach recently demonstrated for the fitting of peptide modified PBI's to identify the presence of multiple aggregate types[11] we find that the spectra of PBI-A at any pH ($A_{pH}(\lambda)$) can be modelled as a linear combination of the spectra at these 3 pH values, Eq. 1.

$$A_{pH}(\lambda) = \sum C_x A_x(\lambda) \quad \text{Eq. 1.}$$

Where C_x is the coefficient of each component spectrum (A_x) corresponding to the type of aggregate present at pH 10 (which we label as type 1), pH 4 (type 2) and pH 2 (type 3), Figure 7b. A plot of C_x versus pH gives an estimate of the relative concentration of each PBI aggregate type, Figure 7c. At the pH values where H_2 evolution occurs the dominant spectral contribution is from type 2 aggregates. The UV-Vis absorption spectra of PBI-V also shows

very similar behaviour with the data being fitted to a combination of 3 contributing spectra (Figure S22). For PBI-V we also find a correlation between level of photocatalytic H_2 evolution and the concentration of an aggregate species that has a UV-Vis spectrum similar to the type 2 form seen with PBI-A.

In contrast, for photocatalytically inactive samples PBI-H and PBI-Y the pH dependent UV-Vis absorption spectra show different pH dependent behaviour and we do not see evidence of the type 2 aggregate that is shown to be photocatalytically active for PBI-A and –V within the UV-Vis spectra of either PBI-Y (Figure 7) or PBI-H (Figure S23). Instead the spectra of PBI-Y can be well fitted to a linear combination of just two spectra (Figure 7e, residual plots and further details of the fitting accompanies S24,25). At high pH (10 to 6), the UV-Vis absorption spectra of PBI-Y 5 mg/ml with 20 v/v% methanol shows a small decrease in the ratio of the first two vibronic peak intensities when compared to a solution of PBI-Y at 10^{-6} M (Figure S26) but minimal broadening and shift in peak positions, indicating weak electronic coupling between PBI sub-units at this pH (type 1', Figure 7d).[47] At the lowest pH studied (pH 2) the UV-Vis spectra of PBI-Y is broadened and under these conditions SAXS experiments show that the PBI aggregates form fibre networks of flexible cylinders (type 3', Figure 7d). Spectra between pH 6 – 2 have an increasing contribution from the type 3' aggregates as the flexible cylinders begin to form at lower pH's. The differences between the UV/Vis spectra of PBI-A and –Y at pH 5 (20% methanol) shows that although both systems forming flexible cylindrical structures the PBI's within these structures are aggregated in different forms.

Figure 8 compares the UV-Vis absorbance spectra of PBI-A at pH 5.0 as the methanol concentration is changed. Again, the spectra can fitted to a linear combination of 3 spectra. SAXS shows that flexible cylinders are present in high levels at all methanol concentrations at pH 5. In agreement with the SAXS data there is only a small contribution to the UV-Vis spectra from the type 1 (small/weakly coupled) aggregates at all methanol concentrations (figure S27). Instead the spectra of PBI-A mainly consist of type 2 and 3 aggregates. A plot of the relative contribution of the type 2 aggregates to the UV-Vis spectrum as the methanol concentration is changed shows excellent agreement to the measured H_2 yield (Figure 8b). The UV-Vis data clearly demonstrates that there is a specific sub-set of PBI-A and -V cylindrical structures with a distinctive UV/Vis spectrum (type 2) that are photocatalytically active which are only formed under certain solvent/pH conditions.

Self-assembly of photoactive units in high dielectric solvents (e.g. water) provides an environment that effectively screens Coulomb potential lowering the energy of long-range charge transfer states (where the exciton is separated not just over the nearest neighbour but over across multiple PBI units). It has been reported that under charge screening conditions mixing of light induced Frenkel excitations, which are typically strongly allowed, and charge

transfer excitations can enable the efficient formation of weakly bound delocalised excitons.[49] This is particularly beneficial for photocatalysis as it enables charge transfer to either the Pt catalyst (electron) or the sacrificial electron donor (hole) and hence efficient photocatalytic H_2 evolution.[36,49] Calculations on face-to-face stacked PMI photocatalysts, similar to the PBI's examined here, have also reported that the UV-Vis absorption spectrum can be used as an indicator of the degree of Frenkel and charge transfer excitation mixing and hence an indicator of ease of electron/hole separation. Systems showing the fastest and most efficient charge separation were characterised by the asymmetry of the absorption line-shape and peak splitting leading to spectral broadening. These reported signatures of strong Frenkel and charge transfer excitation mixing match those observed here in the absorption spectra of the type 2 aggregates of PBI-A and PBI-V that are photocatalytically active. This suggests that through control of pH and methanol content it is possible to tune the local packing of the PBI units within the flexible cylinder leading to the formation of a face-to-face π-aggregated structure that enable efficient charge separation. In contrast, in PBI-Y and –H we see none of the previously described indicators of strong mixing of the Frenkel and charge transfer excitations within the absorption spectrum and it is proposed that excitonic states formed within the flexible cylinders remain localised on PBI units.[49]

Finally, we turn to the pH dependence of the PBI-A and -V photocatalysts between pH 5 and 3. SAXS spectroscopy shows no changes in the supramolecular structure and the UV-Vis spectra indicates that the type 2 aggregation form is present at all these pH values. It is important to consider that the change in pH will also change the surface charge of the structures formed.[50,51] Using NMR spectroscopy we have studied the effect of pH on surface charge by the study of chemical probes (such as Na^+ and dioxane-d_8) that interact with 1D PBI structures that align in the magnetic field as reported previously.[48,50,51] The results (Section 4.6 of the Supporting Information) suggest that the greatest interaction between Na^+ and the 1D structures, and therefore greatest negative surface charge on the structures, is around the apparent pK_a. The apparent pK_a is around pH 5.0 for both PBI-A in-line with the peak of H_2 evolution and the drop in photocatalytic activity mirrors the decrease in surface charge of the photocatalytic structure measured by NMR. It may be that the surface charge plays an additional role facilitating either charge separation, however we see no change in the UV-Vis spectrum. Alternatively, the electron transfer to the Pt co-catalyst may be facilitated by interaction between the charged surface and polar PVP-capped Pt particles.

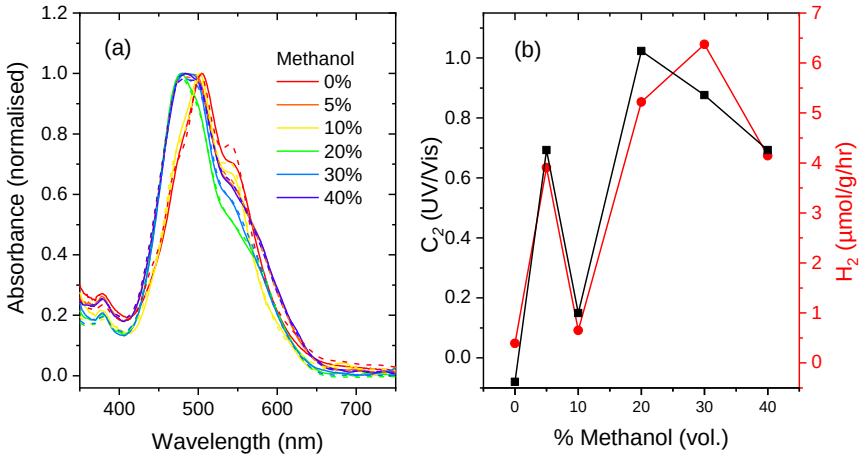

Figure 8. *UV-Vis absorption spectra of (a) PBI-A at pH 5 at a range of methanol concentrations (0% -40 %). Solid lines indicate experimental data, dashed lines are the fit curve generated from a linear combination of the UV-Vis spectra of PBI-A 20 v/v% methanol at pH 2 (type 3), 4 (type 2) and 10 (type 1) using Eq 1. (b) Shows the correlation between the measured H_2 evolution rate (red) with the presence of the type 2 aggregate (black) as the methanol concentration is changed.*

Conclusions

Self-assembled structures represent a greatly underexplored field in photocatalysis. Whilst design of molecular chromophores is commonplace, there has been less attention paid to how these building blocks assemble and the role of the assembly process on photocatalysis. Here we focus, not on achieving record levels of H_2 production, but instead on understanding how and why a single set of starting molecules can give rise to profoundly different levels of photocatalytic activity. The use of high throughput photocatalysis allowed for the simultaneous studies of multiple variables (e.g. pH, solvent mix, PBI functional group) which can all affect the self-assembly process. We completed approximately 350 photocatalysis studies in 2 weeks, in contrast a sample-by-sample approach would have required ~6 months and it is likely that the optimal photocatalysis conditions would not have been discovered without this approach. This is important as it is feasible that viable photocatalysts are being prepared in labs world-wide but discarded after an initial activity analysis with a specific set of conditions showed low levels of activity. Using a combination of SAXS and NMR spectroscopies we have been able to show in our systems that formation of charged flexible cylindrical aggregates is required, but in-itself insufficient, for efficient photocatalysis. This can be rationalised by the clear correlation between UV-Vis spectral features and photocatalytic activity that indicates that a specific form of local packing within the cylindrical aggregates is also essential for

photocatalysis. It appears likely that in this study on supramolecular structures in aqueous solvent that the most active forms are those that lead to strong mixing of the Frenkel and charge transfer excitations. Future modelling and experimental studies will focus on confirming the specific packing motif and its role on the photophysical properties of the material. However, it is already clear that control of the self-assembly process offers an exciting route to tuning activity of photocatalysts for the production of solar fuels

Acknowledgements

Financial support for this works is from the EPSRC (EP/P034497/1, EP/L021978/1) and Leverhulme Trust (RPG-2018-013). MW thanks the Royal Commission for the Exhibition of 1851 for a Research Fellow.

References

1 F. Würthner and M. Stolte, *Chem. Commun.*, 2011, **47**, 5109–5115.

2 D. Görl, X. Zhang and F. Würthner, *Angew. Chemie - Int. Ed.*, 2012, **51**, 6328–6348.

3 F. Würthner, *Chem. Commun.*, 2004, **4**, 1564–1579.

4 S. R. Greenfield, W. A. Svec, D. Gosztola and M. R. Wasielewski, *J. Am. Chem. Soc.*, 1996, **118**, 6767–6777.

5 J. K. Gallaher, E. J. Aitken, R. A. Keyzers and J. M. Hodgkiss, *Chem. Commun.*, 2012, **48**, 7961.

6 E. R. Draper, B. J. Greeves, M. Barrow, R. Schweins, M. A. Zwijnenburg and D. J. Adams, *Chem*, 2017, **2**, 716–731.

7 C. Huang, S. Barlow and S. R. Marder, *J. Org. Chem.*, 2011, **76**, 2386–407.

8 Z. Zhao, Y. Xiao, Y. Zhang and H. Wang, *RSC Adv.*, 2013, **3**, 21373–21376.

9 W. Zhang, Q. Jiang, J. Zhou, D. Hu, X. Zhou, W. Ma, M. Hanif, Z. Xie, L. Liu and Y. Ma, *Sci. China Chem.*, 2017, **60**, 1334–1339.

10 F. Würthner, C. R. Saha-Möller, B. Fimmel, S. Ogi, P. Leowanawat and D. Schmidt, *Chem. Rev.*, 2016, **116**, 962–1052.

11 G. L. Eakins, J. K. Gallaher, R. A. Keyzers, A. Falber, J. E. A. Webb, A. Laos, Y. Tidhar, H. Weissman, B. Rybtchinski, P. Thordarson and J. M. Hodgkiss, *J. Phys. Chem. B*, 2014, **118**, 8642–8651.

12 J. Kiwi, *J. Chem. Soc. Faraday Trans. I*, 1987, **83**, 1101.

13 A. Sharma, J. P. Wojciechowski, Y. Liu, T. Pelras, C. M. Wallace, M. Müllner, A. Widmer-Cooper, P. Thordarson and G. Lakhwani, *Cell Reports Phys. Sci.*, 2020, **1**, 100148.

14 S. Chen, P. Slattum, C. Wang and L. Zang, *Chem. Rev.*, 2015, **115**, 11967–11998.

15 S. Asir, A. S. Demir and H. Icil, *Dye. Pigment.*, 2010, **84**, 1–13.

16 N. P. Brandon and Z. Kurban, *Philos. Trans. R. Soc. A Math. Phys. Eng. Sci.*, , DOI:10.1098/rsta.2016.0400.

17 M. A. Rosen and S. Koohi-Fayegh, *Energy, Ecol. Environ.*, 2016, **1**, 10–29.

18 I. Staffell, D. Scamman, A. Velazquez Abad, P. Balcombe, P. E. Dodds, P. Ekins, N. Shah and K. R. Ward, *Energy Environ. Sci.*, 2019, **12**, 463–491.

19 D. Wang, Y. Zhu, W. Shi, D. Liu, J. Wang and Z. Zhang, *Appl. Catal. B Environ.*, 2016, **202**, 289–297.

20 A. S. Weingarten, R. V Kazantsev, L. C. Palmer, M. McClendon, A. R. Koltonow, A. P. S. Samuel, D. J. Kiebala, M. R. Wasielewski and S. I. Stupp, *Nat. Chem.*, 2014, **6**, 964–970.

21 S. Chen, D. L. Jacobs, J. Xu, Y. Li, C. Wang and L. Zang, *RSC Adv.*, 2014, **4**, 48486–48491.

22 M. C. Nolan, J. J. Walsh, L. L. E. Mears, E. R. Draper, M. Wallace, M. Barrow, B. Dietrich, S. M. King, A. J. Cowan and D. J. Adams, *J. Mater. Chem. A*, 2017, **5**, 7555–7563.

23 T. Abe, K. Nagai, S. Kabutomori, M. Kaneko, A. Tajiri and T. Norimatsu, *Angew. Chemie - Int. Ed.*, 2006, **45**, 2778–2781.

24 H. J. Lee, J. Kim, A. Abudulimu, J. Cabanillas-Gonzalez, P. C. Nandajan, J. Gierschner, L. Lüer and S. Y. Park, *J. Phys. Chem. C*, 2020, **124**, 6971–6978.

25 E. R. Draper, J. J. Walsh, T. O. McDonald, M. A. Zwijnenburg, P. J. Cameron, A. J. Cowan and D. J. Adams, *J. Mater. Chem. C*, 2014, **2**, 5570–5575.

26 T. Tang, J. Qu, K. Müllen and S. E. Webber, *Langmuir*, 2006, **22**, 7610–7616.

27 P. K. Sukul, D. Asthana, P. Mukhopadhyay, D. Summa, L. Muccioli, C. Zannoni, D. Beljonne, A. E. Rowan and S. Malik, *Chem. Commun.*, 2011, **47**, 11858–11860.

28 E. Krieg, E. Shirman, H. Weissman, E. Shimoni, S. G. Wolf, I. Pinkas and B. Rybtchinski, *J. Am. Chem. Soc.*, 2009, **131**, 14365–14373.

29 E. R. Draper, L. J. Archibald, M. C. Nolan, R. Schweins, M. A. Zwijnenburg, S. Sproules

and D. J. Adams, *Chem. - A Eur. J.*, 2018, **24**, 4006–4010.

30 J. J. Walsh, J. R. Lee, E. R. Draper, S. M. King, F. Jackel, M. A. Zwijnenburg, D. J. Adams and A. J. Cowan, *J. Phys. Chem. C*, 2016, **120**, 18479–18486.

31 L. L. E. Mears, E. R. Draper, A. M. Castilla, H. Su, Zhuola, B. Dietrich, M. C. Nolan, G. N. Smith, J. Doutch, S. Rogers, R. Akhtar, H. Cui and D. J. Adams, *Biomacromolecules*, 2017, **18**, 3531–3540.

32 E. R. Draper, L. L. E. Mears, A. M. Castilla, S. M. King, T. O. McDonald, R. Akhtar and D. J. Adams, *RSC Adv.*, 2015, **5**, 95369–95378.

33 C. L. Smith, L. L. E. E. Mears, B. J. Greeves, E. R. Draper, J. Doutch, D. J. Adams and A. J. Cowan, *Phys. Chem. Chem. Phys.*, 2019, **21**, 26466–26476.

34 A. Dannenhoffer, H. Sai, D. Huang, B. Nagasing, B. Harutyunyan, D. J. Fairfield, T. Aytun, S. M. Chin, M. J. Bedzyk, M. Olvera de la Cruz and S. I. Stupp, *Chem. Sci.*, 2019, **10**, 5779–5786.

35 A. S. Weingarten, R. V. Kazantsev, L. C. Palmer, D. J. Fairfield, A. R. Koltonow and S. I. Stupp, *J. Am. Chem. Soc.*, 2015, **137**, 15241–15246.

36 A. S. Weingarten, A. J. Dannenhoffer, R. V. Kazantsev, H. Sai, D. Huang and S. I. Stupp, *J. Am. Chem. Soc.*, 2018, **140**, 4965–4968.

37 H. Sai, A. Erbas, A. Dannenhoffer, D. Huang, A. Weingarten, E. Siismets, K. Jang, K. Qu, L. C. Palmer, M. Olvera De La Cruz and S. I. Stupp, *J. Mater. Chem. A*, 2019, **8**, 158–168.

38 H. Wu, L. Xue, Y. Shi, Y. Chen and X. Li, *Langmuir*, 2011, **27**, 3074–3082.

39 L. Klouda, *Eur. J. Pharm. Biopharm.*, 2015, **97**, 338–349.

40 Z. Y. Ju and A. Kilara, *J. Agric. Food Chem.*, 1998, **46**, 1830–1835.

41 Y. Bai, L. Wilbraham, B. J. Slater, M. A. Zwijnenburg, R. S. Sprick and A. I. Cooper, *J. Am. Chem. Soc.*, 2019, **141**, 9063–9071.

42 Y. Z. Zhao, K. X. Li, S. Y. Ding, M. Zhu, H. P. Ren, Q. Ma, Z. Guo, S. P. Tian, H. Q. Zhang and Z. C. Miao, *Russ. J. Phys. Chem. A*, 2018, **92**, 1261–1265.

43 C. R. Deblase, K. Hernandez-Burgos, J. M. Rotter, D. J. Fortman, D. Dos S. Abreu, R. A. Timm, I. C. N. Diogenes, L. T. Kubota, H. D. Abruna and W. R. Dichtel, *Angew. Chemie - Int. Ed.*, 2015, **54**, 13225–13229.

44 http://www.sasview.org/.

45 A. M. Castilla, E. R. Draper, M. C. Nolan, C. Brasnett, A. Seddon, L. L. E. Mears, N.

Cowieson and D. J. Adams, *Sci. Rep.*, 2017, **7**, 1–10.

46 F. C. Spano, *Acc. Chem. Res.*, 2010, **43**, 429–439.

47 Z. Chen, V. Stepanenko, V. Dehm, P. Prins, L. D. A. Siebbeles, J. Seibt, P. Marquetand, V. Engel and F. Würthner, *Chem. - A Eur. J.*, 2007, **13**, 436–449.

48 E. R. Draper, L. Wilbraham, D. J. Adams, M. Wallace, R. Schweins and M. A. Zwijnenburg, *Nanoscale*, 2019, **11**, 15917–15928.

49 N. J. Hestand, R. V. Kazantsev, A. S. Weingarten, L. C. Palmer, S. I. Stupp and F. C. Spano, *J. Am. Chem. Soc.*, 2016, **138**, 11762–11774.

50 M. Wallace, J. A. Iggo and D. J. Adams, *Soft Matter*, 2017, **13**, 1716–1727.

51 M. Wallace, J. A. Iggo and D. J. Adams, *Soft Matter*, 2015, **11**, 7739–7747.